energies

MDPI

Article

A Bidirectional DHC-LT Resonant DC-DC Converter with Research on Improved Fundamental Harmonic Analysis Considering Phase Angle of Load Impedance

Shuhuai Zhang [1,†], Xuezhi Wu [1,*,†], Ziqian Zhang [2,†] and Xuejiang Zhang [2,†]

[1] Faculty of Electrical Engineering, Beijing Jiaotong University, Beijing 100044, China; zshtjdx@126.com
[2] Beijing Dynamic Power Co., Ltd., Beijing 100070, China; lovedream3000@126.com (Z.Z.); yitianxialearn@126.com (X.Z.)
* Correspondence: xzhwu@bjtu.edu.cn; Tel.: +86-135-0129-1928
† These authors contributed equally to this work.

Abstract: This paper presents a novel 400 V–50 V bidirectional DHC-LT resonant DC-DC converter. By adding a resonant capacitor and an auxiliary transformer based on LLC, zero-voltage switching (ZVS) and zero-current switching (ZCS) are achieved, while the output voltage gain range is broadened in two directions. Operation principles and robustness are discussed with equations. Then, the error factor of fundamental harmonic analysis (FHA) in resonant converters is analyzed. Considering the phase difference between the output voltage and resonant tank current, an improved method is proposed to describe the behavior of the DHC-LT converter more precisely. A comparison is conducted to prove the effectiveness of the proposed FHA. Furthermore, in order to reduce the output voltage and provide a ripple-free charging current, a fixed-frequency phase-shift strategy is introduced in the DHC-LT converter. ZVS can be realized through the reasonable design of dead time and phase-shift angle. Finally, a 2.5 kW prototype of the DHC-LT resonant DC-DC converter with a digital signal processor (DSP) platform and a battery/PV DC test system is established in the lab to validate the theoretical analysis.

Keywords: bidirectional; DHC-LT resonant DC-DC converter; FHA; phase-shift control

check for updates

Citation: Zhang, S.; Wu, X.; Zhang, Z.; Zhang, X. A Bidirectional DHC-LT Resonant DC-DC Converter with Research on Improved Fundamental Harmonic Analysis Considering Phase Angle of Load Impedance. *Energies* **2022**, *15*, 5281. https://doi.org/10.3390/en15145281

Academic Editor: Miguel Castilla

Received: 16 June 2022
Accepted: 15 July 2022
Published: 21 July 2022

Publisher's Note: MDPI stays neutral with regard to jurisdictional claims in published maps and institutional affiliations.

Copyright: © 2022 by the authors. Licensee MDPI, Basel, Switzerland. This article is an open access article distributed under the terms and conditions of the Creative Commons Attribution (CC BY) license (https://creativecommons.org/licenses/by/4.0/).

1. Introduction

At present, many power electronics applications, such as renewable energy storage systems (RESSs), automobiles and microgrids, need bidirectional DC-DC converters (BDCs) to transmit power between two different DC buses [1–8]. Since galvanic isolation is an important security guarantee for many applications, isolated bidirectional DC-DC converters are widely used, which can be classified into two kinds: PWM converters and resonant converters [9]. Many PWM converters benefit from zero-voltage switching (ZVS) and a wide output voltage range [10–15]. Meanwhile, power can be transmitted naturally between the two sides [16–18]. However, as zero-current switching (ZCS) cannot be realized easily in many PWM converters, the switching loss cannot be further reduced. By means of resonance between inductors and capacitors, the AC currents in resonant BDCs present as sinusoidal waveforms. Therefore, ZCS can be realized by reasonable design, and efficiency can be further increased. A large number of resonant BDCs with a wide voltage range have been studied recently [19–24].

Thanks to its excellent features of ZVS and ZCS, LLC has attracted attention [25–27]. However, without magnetic inductance, LLC is a traditional series-resonant DC-DC converter when power is transmitted backward, whose voltage gain cannot be increased further. According to [23], with a new control strategy to increase the output voltage, it is possible to achieve a voltage gain greater than 1. Unfortunately, the efficiency is not high enough. To overcome the disadvantage in backward mode, in [24], an auxiliary inductor

is added between the midpoints of bridge arms to make the topology symmetrical in any operating mode, and the power flow can be automatically switched between forward mode and backward mode. Although the prototype in [24] is 1 kW, a greater power rating needs to be verified. To increase the power rating, a 5 kW CLTC BDC is proposed in [28]. Based on LLC, SRC and CLLC, a new auxiliary transformer and an extra resonant capacitor are added, and the CLTC resonant DC-DC converter can achieve ZVS + ZCS. Furthermore, CLTC can achieve high voltage gain with high power load. Based on CLTC, a bidirectional CDT-LC resonant DC-DC converter is proposed [29]. With a similar structure, the converter achieves a beneficial voltage gain characteristic. A wide output voltage range is obtained within a narrow frequency range. To reduce the resonant tank current, an LLCL-type BDC is proposed in [30]. In the LLCL BDC, an inductor is paralleled with a transformer to participate in the main resonance, while the resonant capacitor is moved to the other side of the resonant inductor to improve the gain curve in backward mode. Unfortunately, the capacitors in CLTC, CDT-LC and LLCL BDCs are all in the LVS of the converter, and their conduction loss is quite big. In addition, they have a large volume, which is not good for power density.

In addition to research in topology, research in the modeling of resonant DC-DC converters needs to be conducted for the design of resonant converters. Time-domain analysis [31–34] and FHA [35–37] are two common methods to analyze resonant DC-DC converters. Using time-domain analysis, the calculation results are more accurate. However, the calculation procedure usually utilizes numerical nonlinear programming techniques to solve state equations, which are complicated and not easy to use in engineering applications. Compared to time-domain analysis, FHA is a rather simple and straightforward approach for modeling. It is proposed in [35] to analyze half-bridge resonant converters. Instead of a square wave, a sine wave of voltage appears on the input side of the resonant tank, and resistance appears on the output side. Considering the effect of the filter in the resonant tank, classical AC analysis techniques are adopted, and the calculation is quite simple. However, when the switching frequency is away from the main resonant frequency, the waveforms in the resonant tank are not an ideal sine wave, which may reduce the estimation accuracy. Therefore, an approximate analysis with modification of equivalent AC resistance for the LLC resonant converter is presented in [36]. The comparison shows that the proposed model predicts gain more accurately in discontinuous mode (DCM), which is quite important in the design. Based on [36], a modified gain model and a corresponding design method are proposed in [37]. Compared with traditional FHA, the resonant factor and the load factor are considered and discussed in detail by combining the time domain and the frequency domain, which improves the accuracy of the gain model. However, in the FHA methods mentioned above, the reactive power of the AC load in the resonant tank has not been included. The phase angle between the fundamental components of the AC output voltage and current has not been taken into consideration. Thus, the behavior of the resonant converter is not properly described.

The main objective of the present work is to derive a novel DHC-LT resonant BDC topology and an improved FHA method for resonant converters. Compared to CLTC or CDT-LC BDC in [28,29], by shifting the position of the resonant capacitor from the LVS to the HVS, the volume and conduction loss of the resonant capacitor can be reduced. The power density and efficiency of the proposed BDC can be further improved, which saves physical space and reduces energy consumption in the DC power systems of buildings and community microgrids. Moreover, to improve the accuracy of FHA, the phase angle of the AC load impedance in the resonant tank is taken into consideration. By calculation of the output voltage in secondary resonance and Fourier decomposition, the fundamental components of the output voltage and current are acquired. Thus, the phase angle of the AC load impedance is acquired. The reactive power of the AC load is described. In this way, the behavior of the DHC-LT BDC can be described more precisely, and the accuracy can be increased further. The comprehension of the FHA methodology is updated in this article, which is significant in the design of resonant converters.

This paper is organized as follows: Section 2 introduces the topology structure and operation principles of the proposed DHC-LT BDC. Section 3 analyzes the error factor of the traditional FHA method and proposes an improved FHA method with modification of the AC load impedance. Section 4 compares the proposed improved FHA with the experimental results, simulation, traditional FHA and FHA with an improved model of the AC port equivalent resistance to prove the effectiveness of the improved FHA in this paper. Section 5 shows the waveforms of the 2.5 kW DHC-LT prototype and PV/battery system, which proves the ZVS + ZCS characteristics and wide voltage gain range. Section 6 concludes this paper.

2. Topology Structure and Characteristics

The topology of the proposed DHC-LT BDC is illustrated and analyzed in this section. Then, the operation principles in step-down mode and step-up mode are given. The following sections are demonstrated based on this section.

2.1. Topology Structure

The topology of the DHC-LT BDC is shown in Figure 1. DHC means double high-voltage side (HVS) capacitors. U_H represents the high-voltage port, referring to the high-voltage lithium battery system or DC bus, while U_L represents the low-voltage DC link voltage. Two full-bridge networks are formed with eight power switches, where M_1, M_2, M_3 and M_4 constitute the high-voltage full bridge, and M_5, M_6, M_7 and M_8 constitute the low-voltage full bridge of the proposed converter. The biggest difference between DHC-LT, CLTC, CDT-LC is the position of C_{r2}. In CLTC or CDT-LC, the resonant capacitor C_{r2} is located in the low-voltage side (LVS) of the resonant tank. In order to reduce conduction loss and improve power density, C_{r2} is placed in the HVS of the resonant tank. The resonant inductor L_r and the resonant capacitor C_{r1} are at the same position as the CLTC or CDT-LC converter. T_1 is the main transformer, similar to the transformer in the LLC resonant converter. The magnetic inductor of T_1, L_{m1}, is used to obtain a voltage gain greater than 1. T_2, the auxiliary transformer, is used to make the resonant tank symmetrical. The symbols of "." mean dotted terminals of T_1, and the symbols of "*" mean dotted terminals of T_2. In this way, the topology can obtain a voltage gain greater than 1 in step-up mode. The DHC-LT converter is modulated with pulse-frequency modulation (PFM). In step-down mode, M_5, M_6, M_7 and M_8 are driven by synchronous rectification (SR). In step-up mode, SR is not used, and antiparallel diodes of M_1–M_4, D_1–D_4, work to realize rectification.

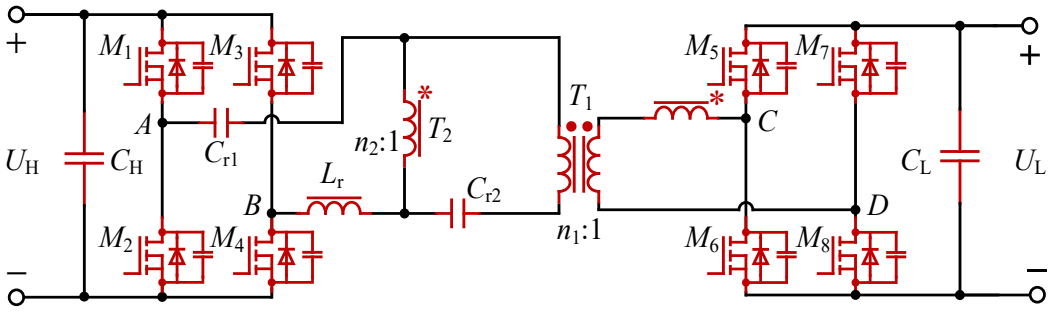


Figure 1. The proposed DHC-LT BDC (The symbols of "*" are dotted terminals of T_2).

2.2. Operation Principles

In order to simplify the analysis, the operation waveforms of currents, voltages and gate signals are depicted in Figure 2. In Figure 2, i_{14} is the drain-source current flowing through M_1 and M_4, i_{23} is the drain-source current flowing through M_2 and M_3, i_{58} is the drain-source current flowing through M_5 and M_8, and i_{67} is the drain-source current flowing through M_6 and M_7. i_{Lm1} is the excitation current of transformer T_1 on the HVS, i_{Lm2} is the excitation current of transformer T_2 on the HVS, i_{Lr} is the current flowing through resonant inductor L_r, i'_{Lm1} is the excitation current of transformer T_1 on the LVS, i'_{Lm2} is the

excitation current of transformer T_2 on the LVS, i_{Cr1} is the current flowing through resonant capacitor C_{r1}, and i_{Cr2} is the current flowing through resonant capacitor C_{r2}. U_{DS14} is the drain-source voltage of M_1 and M_4, U_{DS23} is the drain-source voltage of M_2 and M_3, U_{DS58} is the drain-source voltage of M_5 and M_8, and U_{DS67} is the drain-source voltage of M_6 and M_7. M_1 and M_4 are the driving signals of M_1 and M_4, M_2 and M_3 are the driving signals of M_2 and M_3, M_5 and M_8 are the driving signals of M_5 and M_8, and M_6 and M_7 are the driving signals of M_6 and M_7.

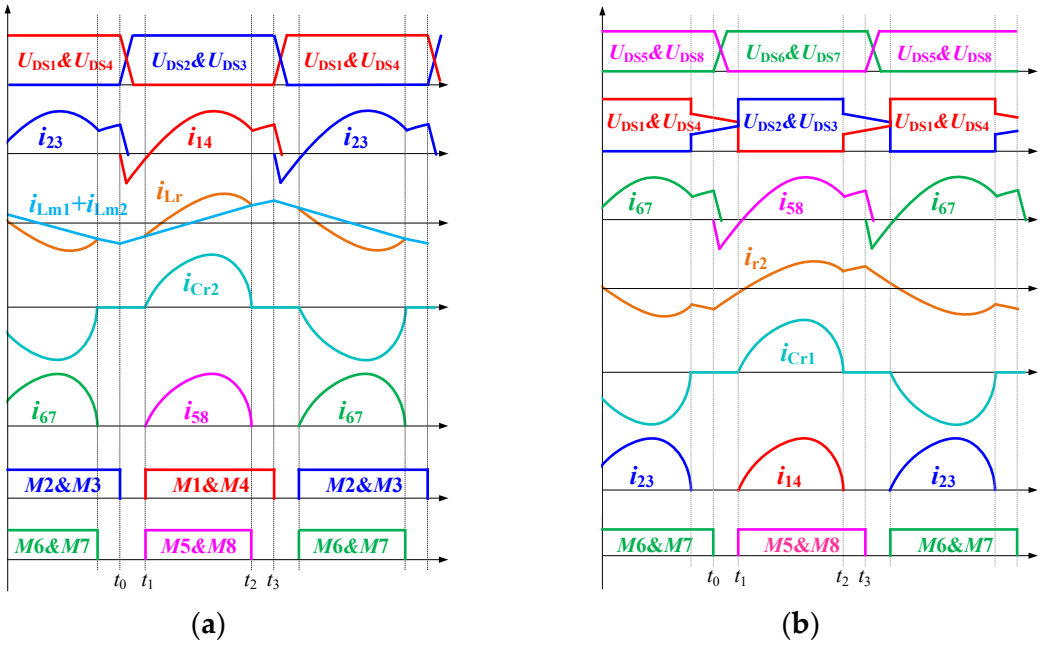


Figure 2. Operation principles of DHC-LT BDC: (**a**) waveforms in step-down mode; (**b**) waveforms in step-up mode.

2.2.1. Step-Down Mode

The equivalent circuits when power flows from the HVS to the LVS are listed in Figure 3. The DHC-LT BDC can work in DCM and continuous current mode (CCM). When the switching frequency is lower than the main resonant frequency and higher than the secondary resonant frequency, DCM appears. On the contrary, the switching frequency is equal to or bigger than the main resonant frequency, and DHC-LT works in CCM. Working in DCM, DHC-LT has three intervals in a half cycle: Intervals A, B and C, as Figure 3 shows. Meanwhile, in CCM, DHC-LT has two intervals: Intervals A and B. Detailed descriptions and explanations of the operational modes in the half period are shown as follows:

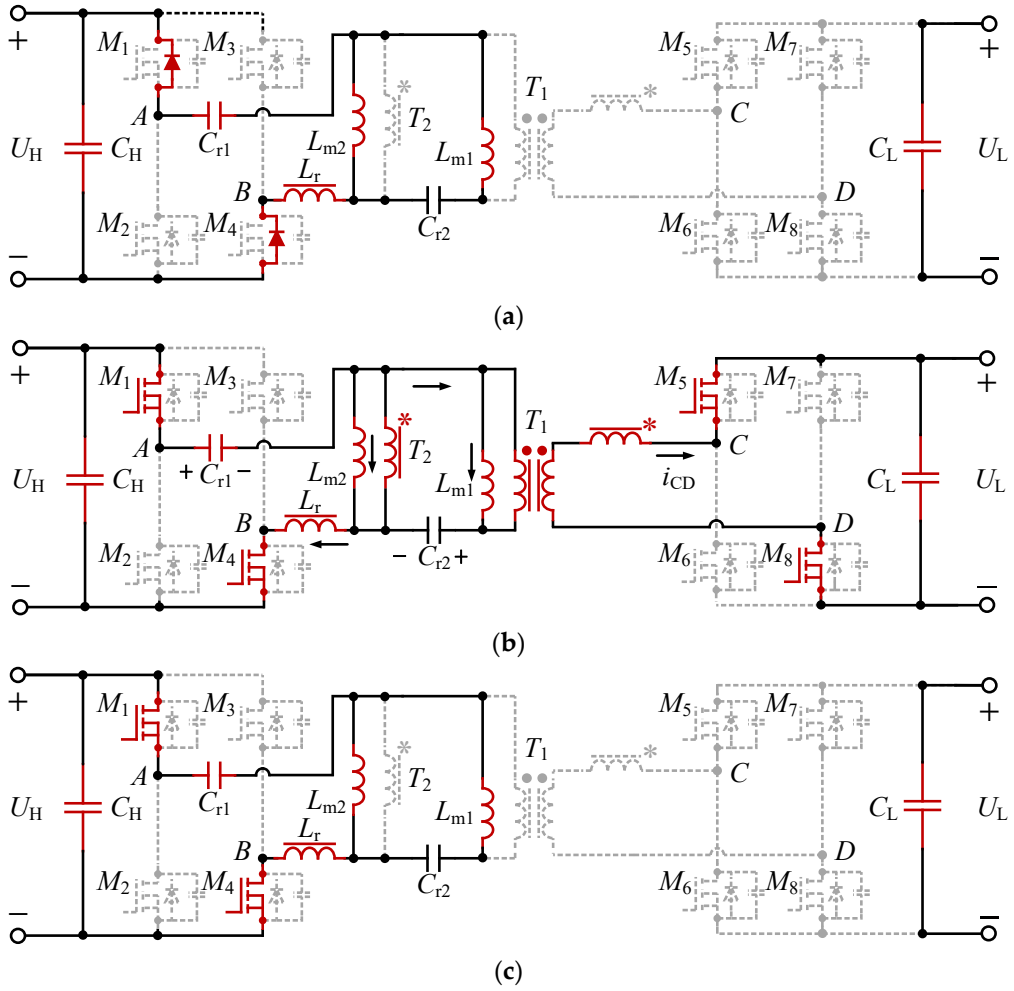


Figure 3. Equivalent circuits in step-down mode: (**a**) Interval A; (**b**) Interval B; (**c**) Interval C (The symbols of "*" are dotted terminals of T_2).

Interval A [t_0–t_1]: This interval is the dead time of the HVS switches. At the beginning of this interval, t_0, M_2 and M_3 are turned off. The HVS resonant current, i_{Lr}, charges the output capacitors of M_2 and M_3 and discharges the output capacitor of M_1 and M_4. Then, the voltage of M_1 and M_4 decreases to 0, and the HVS current passes through the antiparallel diode of M_1 and M_4, which makes the switches turn on under the ZVS condition. The directions of the state variables are shown in Figure 3a. The relevant expressions in this interval are listed below:

$$\begin{cases} u_{DS1}(t) = u_{DS4}(t) = U_H - \frac{C_{r1}}{C_{oss_H}}[u_{Cr1}(t) - u_{Cr1}(t_0)] \\ u_{DS2}(t) = u_{DS3}(t) = \frac{C_{r1}}{C_{oss_H}}[u_{Cr1}(t) - u_{Cr1}(t_0)] \end{cases} \quad (1)$$

Interval B [t_1–t_2]: At t_1, M_1, M_4, M_5 and M_8 turn on, and power is transmitted from the HVS to the LVS. The resonant current changes in a sine wave with main resonant frequency f_r. At t_2, i_{Lr} is equal to the sum of i_{Lm1}, and i_{Lm2}, i_{Cr2} and i_{58} become zero. The directions of the state variables are shown in Figure 3b. The relevant expressions in Interval B are listed below:

$$\begin{cases} C_{r2}\frac{du_{Cr2}(t)}{dt} = i_{Lm1}(t) + \frac{i_{CD}(t)}{n_1} \\ C_{r1}\frac{du_{Cr1}(t)}{dt} = i_{Lr}(t) \\ L_{m1}\frac{di_{Lm1}(t)}{dt} = \frac{-n_1 u_{Cr2}(t) + n_1 n_2 U_L}{n_1 + n_2} \\ L_{m2}\frac{di_{Lm2}(t)}{dt} = \frac{n_2 u_{Cr2}(t) + n_1 n_2 U_L}{n_1 + n_2} \\ Lr\frac{di_{Lr}(t)}{dt} = U_H - u_{Cr1}(t) - \frac{n_2 u_{Cr2}(t) + n_1 n_2 U_L}{n_1 + n_2} \end{cases} \quad (2)$$

Interval C [t_2–t_3]: M_1 and M_4 are still on in this interval, but M_5 and M_8 turn off. As i_{Cr2} and i_{58} are zero in t_2, M_5 and M_8 turn off under the ZCS condition. The HVS goes into secondary resonance with the frequency of $f_{r2d.}$ At t_3, M_1 and M_4 are off, and the dead time begins. The relevant expressions in Interval C are listed below:

$$\begin{cases} C_{r1}\frac{du_{Cr1}(t)}{dt} = i_{Lr}(t) + i_{Lm2}(t) \\ C_{r2}\frac{du_{Cr2}(t)}{dt} = i_{Lr}(t) = i_{Lm1}(t) \\ L_{m2}\frac{di_{Lm2}(t)}{dt} = U_H - u_{Cr1}(t) \\ (L_{m1} + L_r)\frac{di_{Lm1}(t)}{dt} = U_H - u_{Cr1}(t) - u_{Cr2}(t) \end{cases} \quad (3)$$

2.2.2. Step-Up Mode

The equivalent circuits in step-up mode are listed in Figure 4. Similar to step-down mode, DHC-LT can work in CCM mode and DCM mode. Interval C disappears when the working frequency is higher than the main resonant frequency. The corresponding waveforms are described as follows:

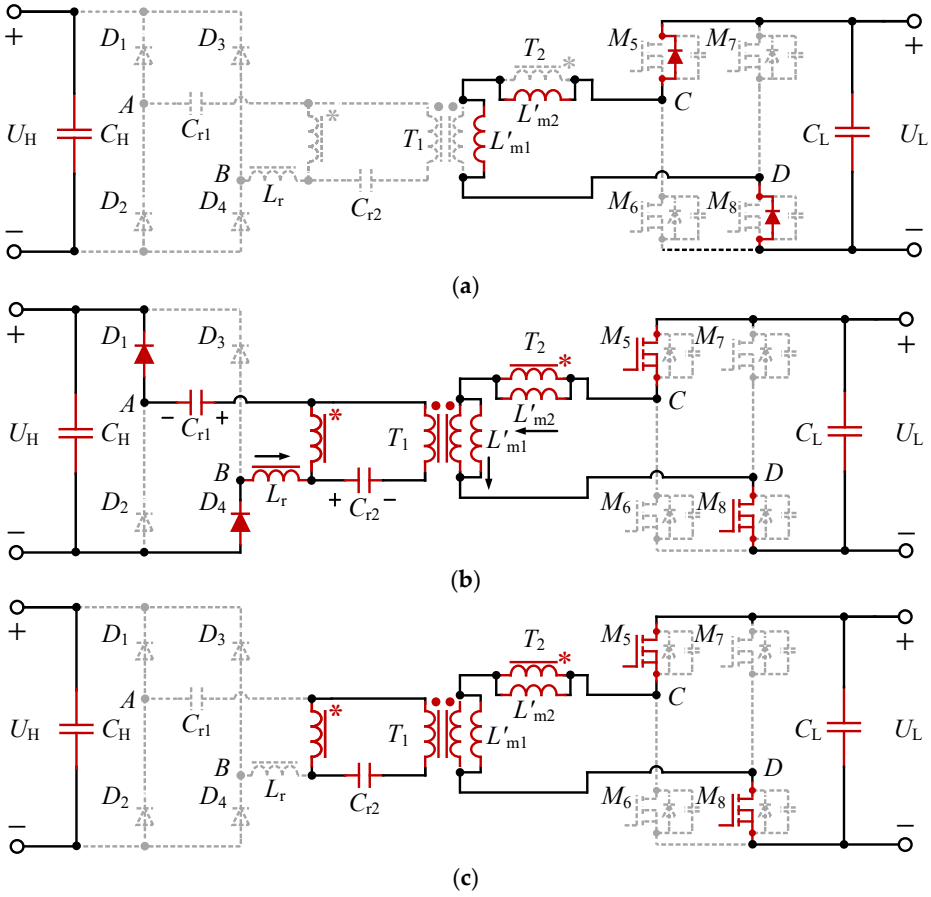


Figure 4. Equivalent circuits in step-up mode: (**a**) Interval A; (**b**) Interval B; (**c**) Interval C (The symbols of "*" are dotted terminals of T_2).

Interval A [t_0–t_1]: This interval begins at t_0 when M_6 and M_7 turn off. During this interval, the parasite capacitors of M_5 and M_8 charge while those of M_6 and M_7 discharge. When the capacitors complete charging and discharging, the LVS current passes through the antiparallel diode of M_5 and M_8. The relevant expressions in this interval are listed below:

$$\begin{cases} u_{DS5}(t) = u_{DS8}(t) = U_L - \frac{\int_{t0}^{t} i'_{Lm1}(x)dx}{C_{oss_L}} \\ u_{DS6}(t) = u_{DS7}(t) = \frac{\int_{t0}^{t} i'_{Lm1}(x)dx}{C_{oss_L}} \end{cases} \quad (4)$$

Interval B [t_1–t_2]: M_5 and M_8 turn on under ZVS at t_1; D_1 and D_4 also turn on, and power is transmitted from the LVS to the HVS. The resonant current on the LVS changes in a sine wave until t_2. The relevant expressions in this interval are listed below:

$$\begin{cases} C_{r1}\frac{du_{Cr1}(t)}{dt} = \left(1+\frac{n_1}{n_2}\right)i_{Lr}(t) + \frac{1}{n_2}[i_{L'm1}(t) - i_{L'm2}(t)] \\ C_{r2}\frac{du_{Cr2}(t)}{dt} = i_{Lr}(t) \\ L'_{m2}\frac{di_{L'm2}(t)}{dt} = \frac{1}{n_2}[U_H + u_{Cr1}(t)] \\ L'_{m1}\frac{di_{L'm1}(t)}{dt} = U_L - \frac{1}{n_2}[U_H + u_{Cr1}(t)] \\ L_r\frac{di_{Lr}(t)}{dt} = n_1\left[U_L - \frac{1}{n_2}U_H - \frac{1}{n_2}u_{Cr1}(t)\right] - U_H - u_{Cr1}(t) - u_{Cr2}(t) \end{cases} \quad (5)$$

Interval C [t_2–t_3]: M_5 and M_8 are still on in this interval, but no power is transmitted from the LVS to the HVS. The LVS goes into secondary resonance with the frequency of f_{r2u}. The resonant tank is rebuilt by C_{r2}, T_1 and T_2. The output current is supplemented by capacitor C_H. Since no current flows through the diodes of the HVS, the switch voltages at the HVS are clamped to $U_H/2$. The relevant expressions in this interval are listed below:

$$\begin{cases} C_{r1}\frac{du_{Cr1}(t)}{dt} = 0 \\ C_{r2}\frac{du_{Cr2}(t)}{dt} = i_{Lr}(t) = -i_{L'm2}(t) \\ L'_{m2}\frac{di_{L'm2}(t)}{dt} = \frac{n_1U_L - U_{Cr2}}{n_1+n_2-\frac{L_r}{L'_{m2}}} \\ L'_{m1}\frac{di_{L'm1}(t)}{dt} = U_L - \frac{n_1U_L - U_{Cr2}}{n_1+n_2-\frac{L_r}{L'_{m2}}} \end{cases} \quad (6)$$

2.3. Simulation Verification

A simulation in PSIM software is used to verify the analysis. In PSIM, idealized components are used to build circuits, and the trapezoidal method is adopted to solve system equations. In this way, the simulation velocity is increased, and the robustness of the simulation is improved. Figure 5 shows the simulation model of the DHC-LT BDC. R_{mos_H}, R_{mos_L}, R_{Cr1}, R_{Cr2}, R_{Lr}, R_{T1_H}, R_{T2_H}, R_{T1_L}, R_{T2_L}, ESR_{CH} and ESR_{CL} are the resistances of the components. In Figure 6a,b and Figure 7a,b, the waveforms in two directions are shown, proving that secondary resonance exists in DCM mode. The output voltages V_{CD} and V_{AB} are not clamped to U_L and U_H when secondary resonance appears. On the contrary, in Figures 6c and 7c, when the switching frequency increases beyond the main resonant frequency, the resonant currents in the tank, i_{AB} and i_{CD}, are continuous. V_{CD} and V_{AB} are clamped to U_L and U_H in the half period.

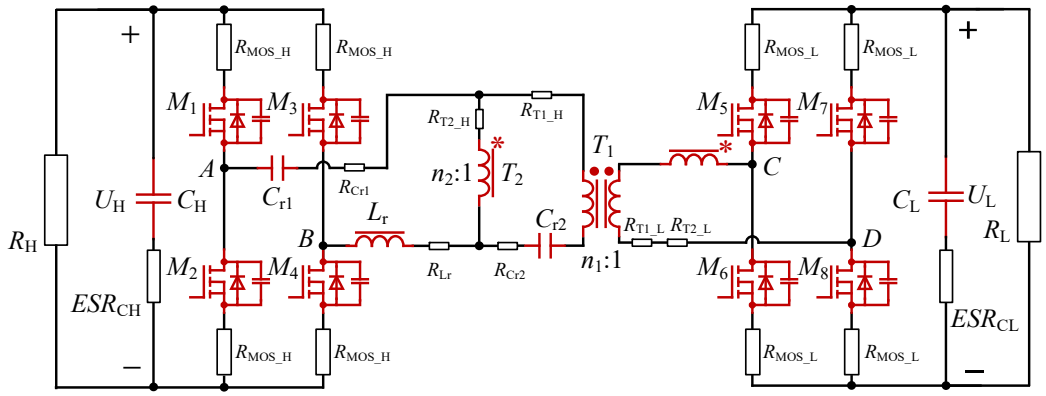
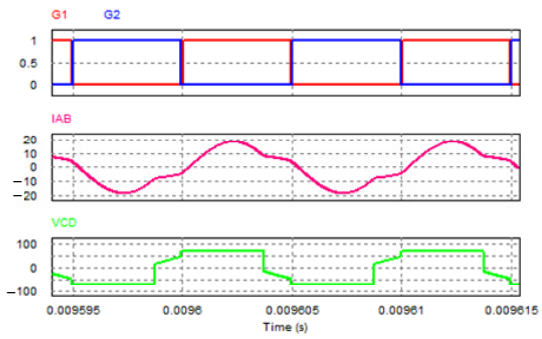
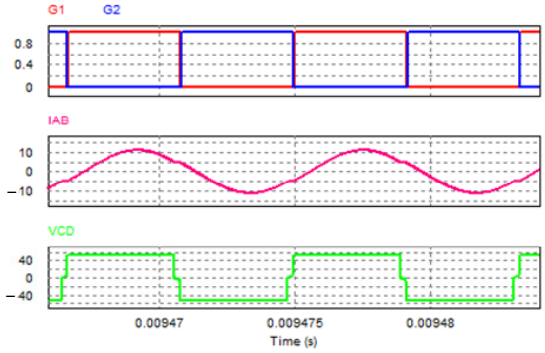


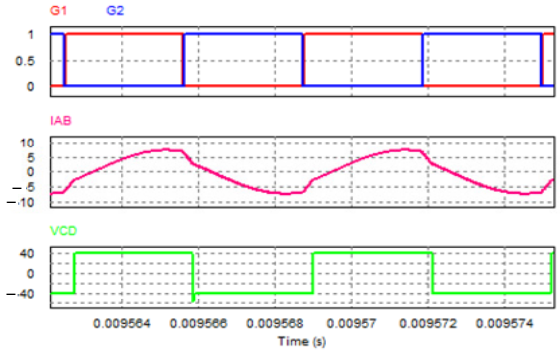
Figure 5. Simulation model for DHC-LT BDC (The symbols of "*" are dotted terminals of T_2).



(**a**)

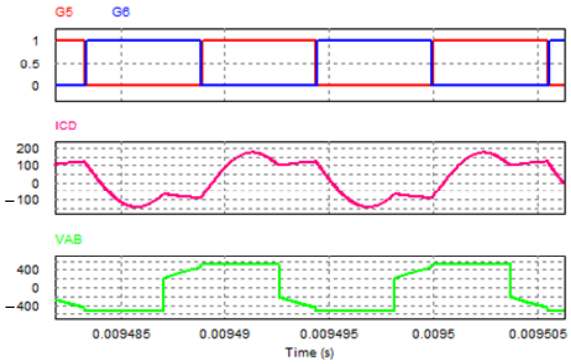


(**b**)

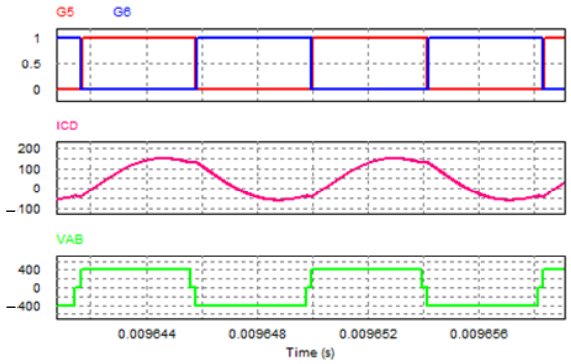


(**c**)

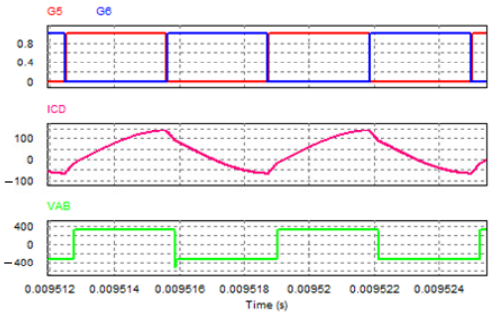
Figure 6. Simulation waveforms in step-down mode, 400 V, 1 Ω: (**a**) 90 kHz; (**b**) 120 kHz; (**c**) 160 kHz.



(**a**)



(**b**)



(**c**)

Figure 7. Simulation waveforms in step-up mode, 50 V, 64 Ω: (**a**) 100 kHz; (**b**) 120 kHz; (**c**) 160 kHz.

2.4. Small-Signal Modeling

By applying the EDF concept and derivation procedures in [27] to the DHC-LT resonant converter, the small-signal mode is illustrated in this section. The open-loop transfer function from the control to the output voltage is shown in List 1 of the Appendix A. As shown in Figure 8, the low-frequency gain is about −55 dB, so the robustness of the proposed converter is strong, but the dynamic response is slow, which is similar to the LLC resonant converter. As the two sides of the DHC-LT converter are controlled by other converters or clamped by batteries, the fast dynamic response of the DHC-LT converter is not needed to make the DC power system stable, so it can be inferred that the DHC-LT converter is suitable in the DC power use of buildings and community microgrids.

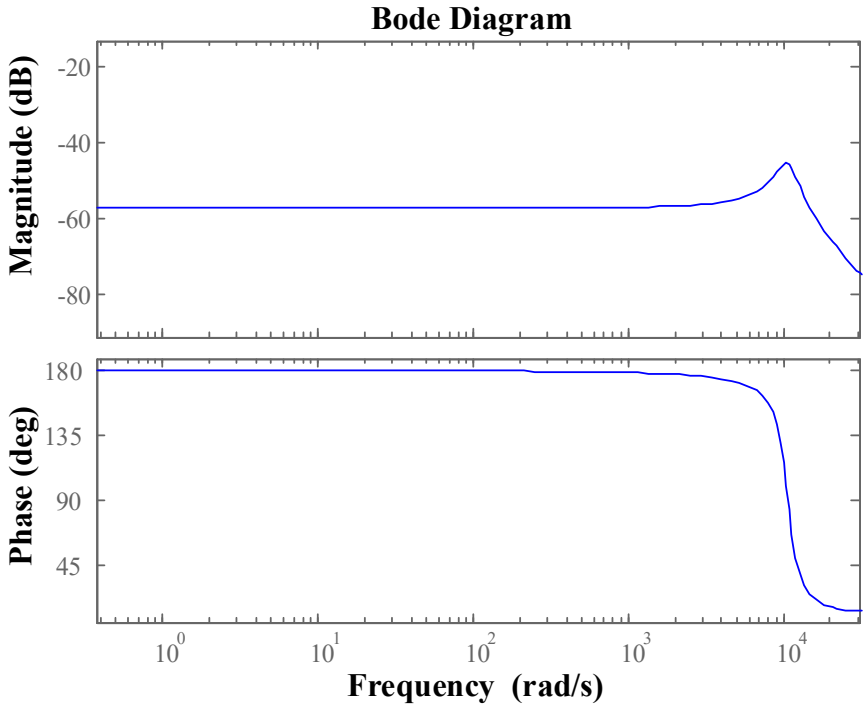


Figure 8. Transfer function from control to output voltage.

3. Improved FHA with Modification of AC Load Impedance

In this section, an improved FHA method is proposed to improve the accuracy of calculation. The main work is modifying the AC load impedance in the FHA, considering the phase angle of the AC load.

Traditional FHA is a simple and direct method to calculate voltage gain, which is essential for the design of resonant DC-DC converters, such as LLC and series-resonant converters. Compared to traditional FHA, the improved FHA method establishes the fundamental waveforms of the AC output voltage and current in DCM mode. Thus, the phase angle of the AC load impedance is obtained by Fourier decomposition and taken for calculation. The procedure of the improved FHA is: (1) calculate the output voltage of the resonant tank in Interval C, U_{SD} or U_{SU}; (2) extract the fundamental components of the output voltage and current; (3) compute the output impedance of the resonant tank considering its phase angle; (4) calculate the new DC voltage gain using the output impedance in (3) as the AC output load.

3.1. Improved FHA in Step-Down Mode

The equivalent FHA circuit in step-down mode is shown in Figure 9, and relevant waveforms are shown in Figure 10.

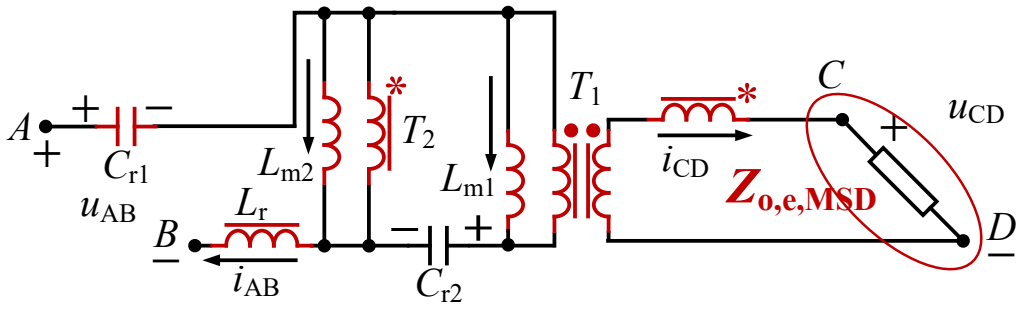


Figure 9. Equivalent FHA circuit in step-down mode (The symbols of "*" are dotted terminals of T_2).

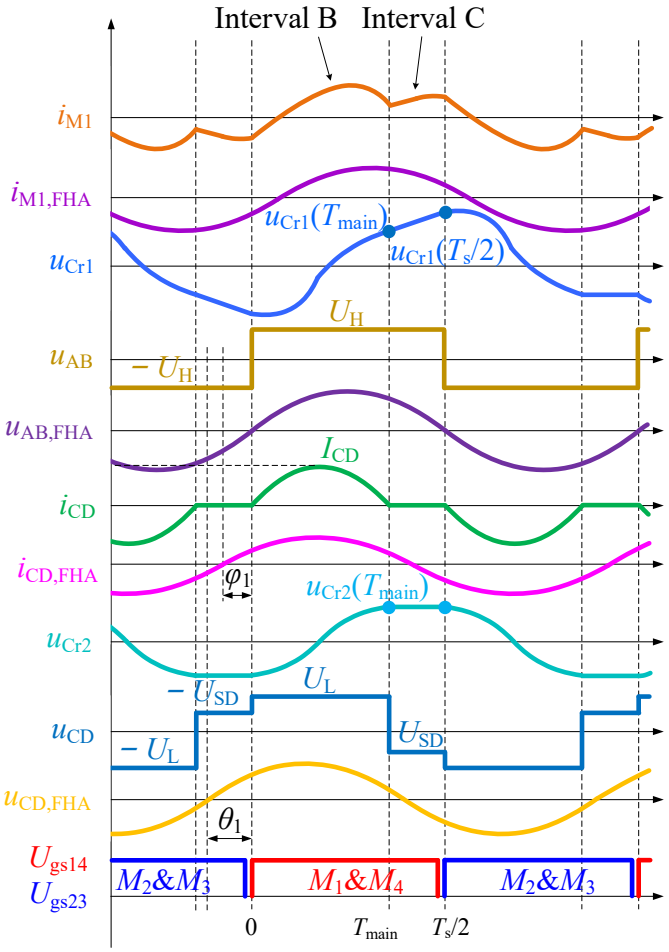


Figure 10. Waveforms in step-down mode.

Assuming

(a) The main resonance interval (Interval B) lasts half of the main resonant period, and T_{main} is equal to $1/2f_r$.
(b) In Interval C, the voltage between the neutral points of the two arms of the rectifier bridge remains constant, U_{SD}. The current flowing through L_{m1} remains constant, I_{Lm1}, and the current flowing through L_{m2} remains constant, I_{Lm2}.
(c) The efficiency of the DHC-LT resonant circuit is 100%.

The output voltage of the resonant tank in T_{main}, U_{SD}, is shown in List 2 of the Appendix A.

With the method of Fourier decomposition, the angle between the fundamental wave of the output AC current i_{CD} and the fundamental wave of the input AC voltage u_{CD}, φ_1, is estimated as

$$\varphi_1 = \frac{\pi}{2}\left(1 - \frac{f_s}{f_r}\right) \tag{7}$$

The angle between the fundamental wave of the output AC voltage u_{CD} and the fundamental wave of the input AC voltage u_{AB}, θ_1, is estimated as

$$\theta_1 = \arctan\left(\frac{U_L A_1 + U_{SD} B_1}{U_L C_1 + U_{SD} D_1}\right) \tag{8}$$

In the above equation

$$\begin{aligned} A_1 &= \tfrac{2\sin(2\pi f_s \cdot T_{main})}{\pi} \\ B_1 &= -\tfrac{2\sin(2\pi f_s \cdot T_{main})}{\pi} \\ C_1 &= \tfrac{2-2\cos(2\pi f_s \cdot T_{main})}{\pi} \\ D_1 &= \tfrac{2+2\cos(2\pi f_s \cdot T_{main})}{\pi} \end{aligned} \tag{9}$$

Therefore, the output AC impedance is

$$Z_{o,e,MSD} = R'_{o,e,MSD} + j \cdot R'_{o,e,MSD} \cdot \tan(\theta_1 - \varphi_1) \tag{10}$$

$R'_{o,e,MSD}$ is obtained by Reference [36]. $R_{o,SD}$ is the DC load in step-down mode.

$$R'_{o,e,MSD} = \frac{n^2 R_{o,SD}}{2} \frac{\left[1 - \left(\frac{f_s}{f_r}\right)^2\right]^2}{\cos^2\left(\frac{f_s}{f_r}\right)} \tag{11}$$

The RMS value of the output AC peak voltage, $U_{CD,FHA}$, is expressed as

$$U_{CD,FHA} = U_{CD}\sqrt{\left(A_1 + \frac{U_{SD}}{U_L} B_1\right)^2 + \left(C_1 + \frac{U_{SD}}{U_L} D_1\right)^2} \tag{12}$$

The RMS value of the input AC peak voltage u_{AB}, FHA, is expressed as

$$U_{AB,FHA} = \frac{4}{\pi} U_{AB} \tag{13}$$

The modified voltage conversion ratio is

$$\begin{aligned} M_{SD} &= \frac{U_{CD}}{U_{AB}} = \frac{U_{CD}}{U_{CD,FHA}} \frac{U_{CD,FHA}}{U_{AB,FHA}} \frac{U_{AB,FHA}}{U_{AB}} \\ &= \frac{4\left\| \frac{H_1}{sC_{r1}} + sL_r H_1 + sL_{m2} G_1 \right\|}{\pi\sqrt{\left(A_1 + \frac{U_{SD}}{U_L} B_1\right)^2 + \left(C_1 + \frac{U_{SD}}{U_L} D_1\right)^2}} \end{aligned} \tag{14}$$

In the above equation

$$\begin{aligned} E_1 &= \tfrac{s \cdot (1 + n_1/n_2) L_{m1} + {n_1}^2 Z_{o,e,MSD}}{s^2 \cdot n_1 C_{r2} (1 + n_1/n_2) L_{m1} + {n_1}^2 / n_2} \\ F_1 &= \tfrac{-n_1 U_{Cr2}/n_2 + n_1 Z_{o,e,MSD}}{s(1 + n_1/n_2) L_{m1}} \\ G_1 &= \tfrac{U_{Cr2} + n_1 Z_{o,e,MSD}}{s(1 + n_1/n_2) L_{m2}} \\ H_1 &= F_1 + G_1 + 1/n_1 + 1/n_2 \end{aligned} \tag{15}$$

3.2. Improved FHA in Step-Up Mode

The equivalent FHA circuit in step-up mode is shown in Figure 11, and relevant waveforms are shown in Figure 12.

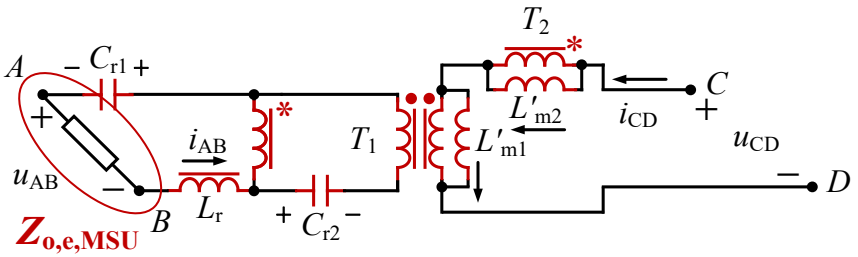


Figure 11. Equivalent FHA circuit in step-up mode. (The symbols of "*" are dotted terminals of T_2).

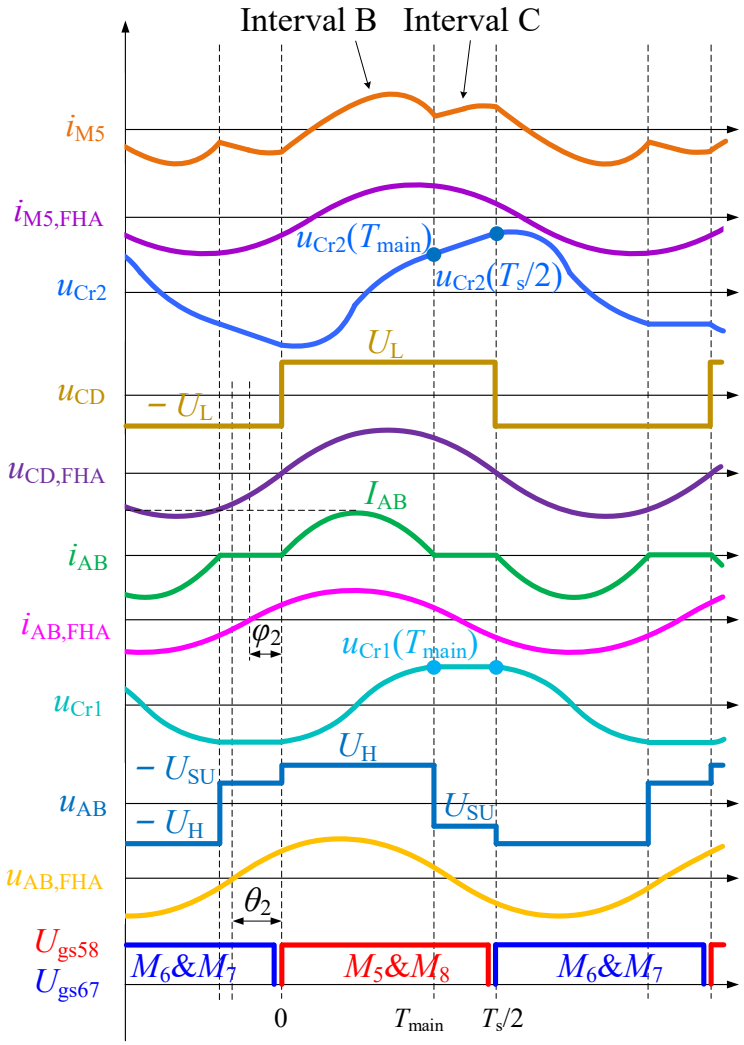


Figure 12. Waveforms in step-up mode.

The output voltage of the resonant tank in T_{main}, U_{SU}, is shown in List 3 of the Appendix A.

With the method of Fourier decomposition, the angle between the fundamental wave of the output AC current i_{AB} and the fundamental wave of the input AC voltage u_{AB}, φ_2, is estimated as

$$\varphi_2 = \frac{\pi}{2}\left(1 - \frac{f_s}{f_r}\right) \tag{16}$$

The angle between the fundamental wave of the input AC voltage u_{CD} and the fundamental wave of the output AC voltage u_{AB}, θ_2, is estimated as

$$\theta_2 = \arctan\left(\frac{U_H A_1 + U_{SU} B_1}{U_H C_1 + U_{SU} D_1}\right) \tag{17}$$

Therefore, the output AC impedance in the HVS is

$$Z_{o,e,MSU} = R'_{o,e,MSU} + j \cdot R'_{o,e,MSU} \cdot \tan(\theta_2 - \varphi_2) \tag{18}$$

$R'_{o,e,MSU}$ is obtained by Reference [36]. $R_{o,SU}$ is the DC load in step-up mode.

$$R'_{o,e,MSU} = \frac{n^2 R_{o,SU}}{2} \frac{\left[1 - \left(\frac{f_s}{f_r}\right)^2\right]^2}{\cos^2\left(\frac{f_s}{f_r}\right)} \tag{19}$$

The modified voltage conversion ratio is

$$M_{SU} = \frac{U_{AB}}{U_{CD}} = \frac{4\left\| \frac{Z_{o,e,MSU}}{\frac{I_1 + J_1}{n_1} + \frac{I_1}{n_2}} \right\|}{\pi\sqrt{\left(A_1 + \frac{U_{SU}}{U_H} B_1\right)^2 + \left(C_1 + \frac{U_{SU}}{U_H} D_1\right)^2}} \tag{20}$$

In the above equation

$$\begin{aligned} I_1 &= \tfrac{1}{sC_{r1}} + sL_r + Z_{o,e,MSU} \\ J_1 &= \frac{n_2 + \frac{I_1}{sn_2 L'_{m2}} - \frac{I_1}{sn_1 L'_{m1}}}{(n_1 + n_2) sC_{r2} + \frac{1}{sn_1 L'_{m1}}} \end{aligned} \tag{21}$$

4. Comparison of Different Modeling Approaches

In order to prove the effectiveness of the improved FHA method proposed in this paper, the methods of the experiment, the improved FHA in this paper, traditional FHA, FHA with an improved model of the AC port equivalent resistance in [36] and simulation are used simultaneously. The simulation results almost coincide with the experimental results, which means that the simulation model is effective. The parameters of the experimental prototype are listed in Section 5. In Figures 13 and 14, the errors between the experimental results and other methods are minimum around the main resonant frequency. The reason is that, when the DHC-LT converter is working around the main resonant frequency, resonant voltages and resonant currents in the tank are sinusoidal waveforms, and nearly no distortion exists. As the working frequency is reduced, the methods of traditional FHA and FHA with the improved model of the AC port equivalent resistance have a major error. However, when the phase angle of the AC load is considered, in Figure 13, from 80 kHz to 120 kHz, the biggest error between the improved FHA in this paper and the experimental results is around 9%, less than the other methods. Similarly, in Figure 14, from 80 kHz to 120 kHz, the biggest error between the improved FHA in this paper and the experimental results is around 10%. The working frequencies under the peak voltage gain in the improved FHA and experiments are almost the same. The theoretical work is verified by experiments and found to be in good agreement. Therefore, the improved FHA method in Section 3 of this paper is effective in describing the gain characteristics of the DHC-LT converter.

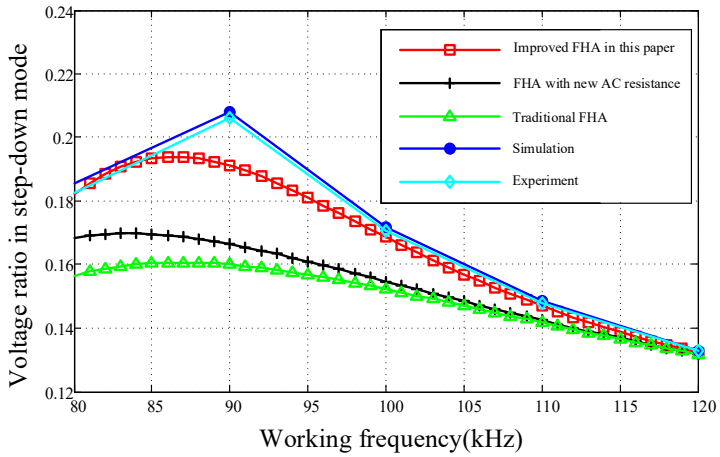


Figure 13. Voltage gain in step-down mode.

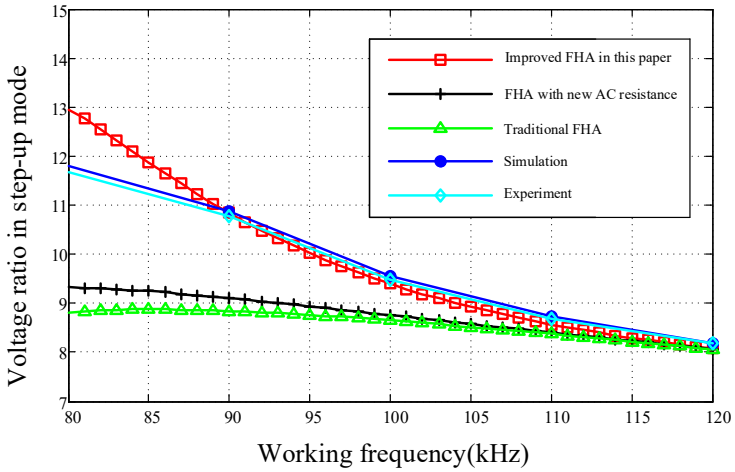


Figure 14. Voltage gain in step-up mode.

5. Experimental Results

A 2.5 kW experimental prototype was established in the lab. Table 1 shows its parameters. A DSP of TMS320F280048 is used to control the proposed DHC-LT converter. To realize ZVS, L_{m1} and L_{m2} are set comparatively small. The power is transmitted mainly from T_1, so the ratio of T_1 is mainly designed by the voltage gain of the converter. As a result, n_1 is significantly smaller than n_2. Compared to CDT-LC, the capacitance of C_{r2} is much smaller than that of the LVS resonant capacitor, which is 4.5 μF in [29]. The MOSFET on the HVS, SRC60R022FB, has a fast-recovery body diode, which is an advantage when power is transmitted from the LVS to the HVS. The MOSFET on the LVS, FDP2D3N10C, is used as a synchronous rectifier to attain higher efficiency.

Table 1. Parameters of the DHC-LT converter.

Component	Model/Value
M_1,M_2,M_3,M_4	SRC60R022FB
M_5,M_6,M_7,M_8	2 paralleled FDP2D3N10C
C_{r1}	108 nF
C_{r2}	36 nF
L_{m1}	160 μH
n_1	10
L_{m2}	80 μH
n_2	18
L_r	40 μH

5.1. Experimental Results of Steady-State Operation

Figure 15 shows the experimental results of the prototype converter. In Figure 15, U_{gs1} is the drive signal of M_1, U_{ds1} is the D-S voltage of M_1, U_{gs5} is the drive signal of M_5, U_{ds5} is the D-S voltage of M_5 and i_{Lr} is the current of the resonant inductor.

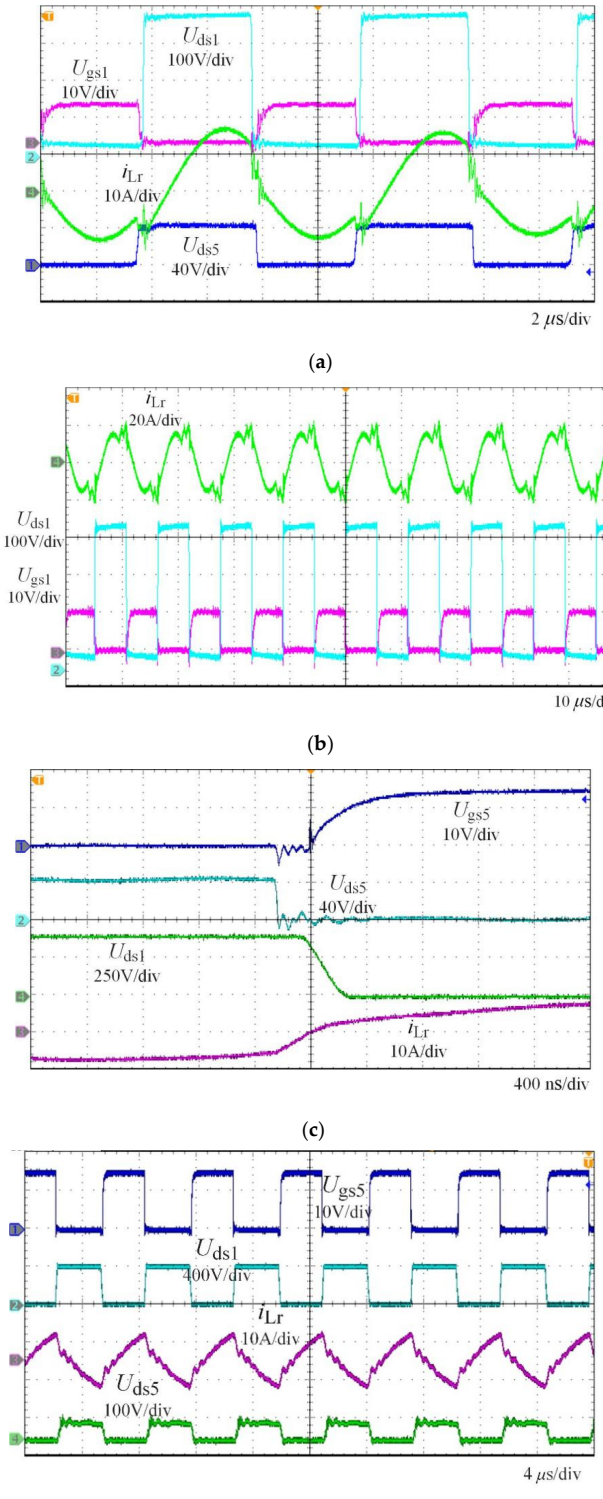


Figure 15. Experimental results of the prototype converter: (**a**) working frequency is 125 kHz, and load is 1 Ω, step-down mode; (**b**) working frequency is 90 kHz, and load is 2.5 Ω, step-down mode (**c**) ZVS in step-up mode; (**d**) working frequency is 160 kHz, and load is 1.4 Ω, step-down mode.

Figure 15a,b shows the experimental results in step-down mode. In Figure 15a, the working frequency is around 125 kHz, which is the main resonant frequency. Therefore, the currents in the resonant tank are almost sinusoidal, which is determined by the designed resonant network. In Figure 15b, the working frequency is around 90 kHz, and secondary resonance happens when the main resonance ends.

Figure 15c,d shows the experimental results in step-up mode. In Figure 15c, ZVS is realized. U_{ds5} decreases to 0, before U_{gs5} comes. The dead time of 300 ns in this prototype is wide enough for both the HVS and LVS power switches, while the efficiency is not affected. In Figure 15d, as the working frequency is higher than the main resonant frequency, secondary resonance does not exist, which is consistent with Section 2.2.2.

The efficiency curves of the DHC-LT converter are shown in Figure 16, which were obtained by experiments. In step-down mode, the peak efficiency is 97.3% when the LVS voltage is 50 V, while the efficiency with 100% load is 96.8%. In step-up mode, the peak efficiency is 97.4% when the LVS voltage is 50 V, while the efficiency with 100% load is 95.7%. The resonant capacitor C_{r2} is moved from the LVS to the HVS, and the heat it produces decreases. As a result, it can be seen that the efficiency of the 2.5 kW DHC-LT converter is higher than that of the 2.5 kW CDT-LC in step-down mode [29]. The advantage of DHC-LT is shown through comparison.

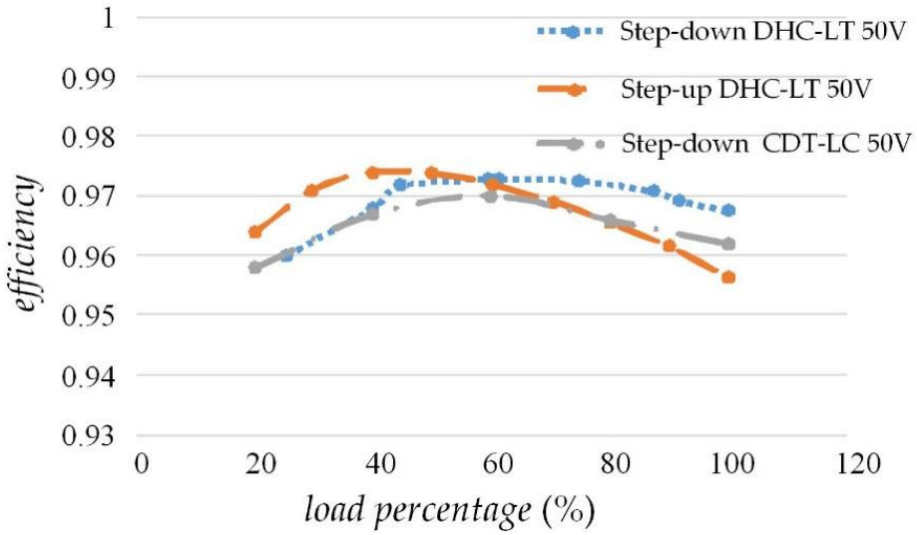


Figure 16. Efficiency curves of DHC-LT and CDT-LC.

5.2. Discussion of Phase-Shift Control

In order to reduce the output voltage, broaden the output voltage range and provide a ripple-free charging current for batteries, a fixed-frequency phase-shift strategy is introduced according to the DHC-LT converter [38]. When the voltage gain is high, traditional PFM control is adopted. The gate signals of M_1 and M_4 are the same. M_1 and M_2 conduct alternately, as do M_3 and M_4. When the voltage gain decreases, the switching frequency increases until it reaches its upper limit, 200 kHz. Then, as shown in Figure 17, when the fixed-frequency phase-shift strategy is adopted in step-down mode, the switching frequency remains constant, and the phase angle between gate signals of M_1 and M_4, M_2 and M_3 increases. When the phase angle increases, the RMS of the input voltage of resonant tank u_{AB} decreases. As a result, the voltage gain is further reduced compared to eht traditional PFM control.

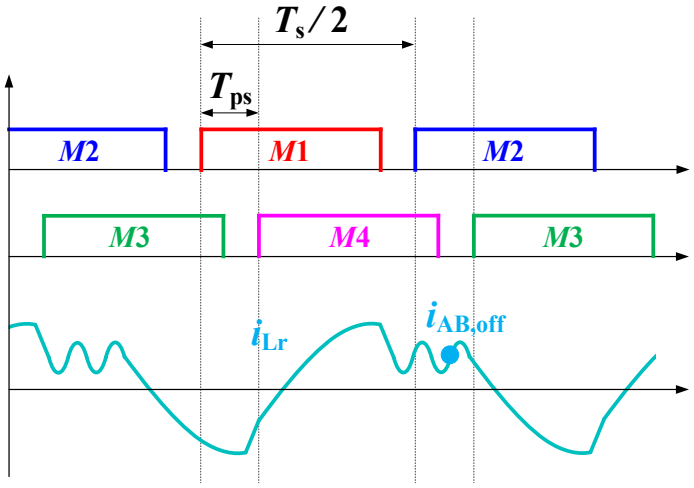


Figure 17. Schematic diagram using fixed-frequency phase-shift strategy in step-down mode.

In Figure 17, as the turn-off current of the leading leg, M_1 and M_2, is higher than that of the lagging leg, M_3 and M_4, in order to guarantee ZVS of four MOSFETs, the dead time of the HVS MOSFETs should meet the requirement

$$t_{dt_SD} \geq \frac{4\int_0^{UH} C_{oss_H} du_{AB}}{i_{AB,off}} \tag{22}$$

$i_{AB,off}$ can be obtained when the voltage of C_{r1} and C_{r2} is 0.

$$i_{AB,off} = \frac{U_H\left(\frac{T_s}{2} - T_{ps}\right)}{2\left(L_r + \frac{L_{m1}L_{m2}}{L_{m1}+L_{m2}}\right)} \tag{23}$$

Figure 18 shows the waveforms using the fixed-frequency phase-shift strategy in step-down mode. i_{Lr} decreases when MOSFETs on the leading leg turn off and MOSFETs on the lagging leg turn on. The working frequency reaches its upper limit, 200 kHz. ZVS is realized as the phase-shift angle is small.

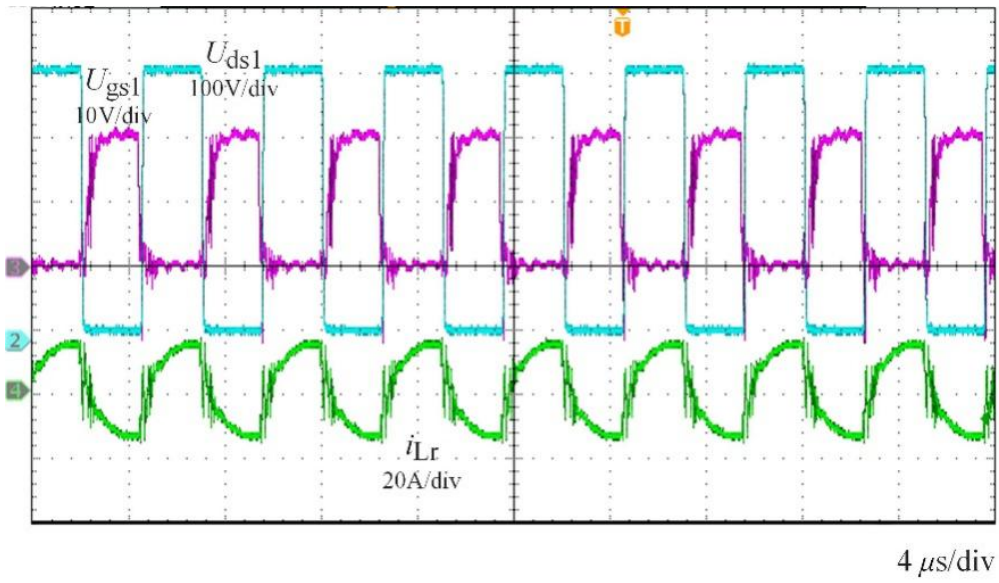


Figure 18. Waveforms using fixed-frequency phase-shift strategy in step-down mode.

5.3. Verification in Battery/PV System

To verify the proposed DHC-LT converter in a battery/PV system, the battery/PV test system diagram is shown in Figure 19. In Figure 19a, the maximum power point tracking (MPPT) DC-DC converter and the DHC-LT bidirectional DC-DC converter transfer the energy from the PV and batteries to the 400 V DC bus. The power PV generated is stored in batteries and expended in the DC load. When the DC load is heavier than the power PV generated, the batteries start to release power to the DC bus and the DC load. Figure 19b shows the prototype of the DC power system, which consists of the MPPT DC-DC converter, the DHC-LT DC-DC converter and their control system. In Figure 19c, one DC source is used to simulate PV, while the other electronic load is used as the DC load on the 400 V bus. They are both controlled by the host computer on the desk.

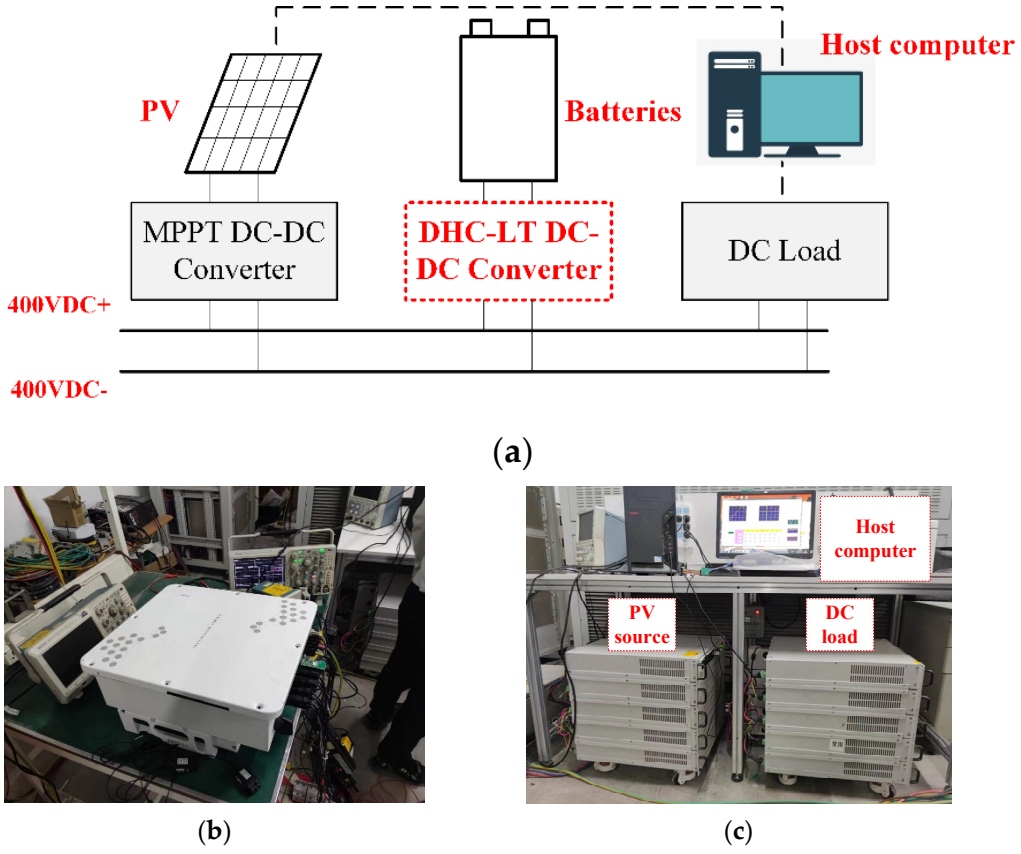


Figure 19. Diagram of battery/PV test system: (**a**) schematic diagram of the whole DC test power system; (**b**) prototype of DC power system; (**c**) DC source, DC load and host computer.

Waveforms in the battery/PV test system are shown in Figure 20. Figure 20a,b shows the variation of battery voltage U_{bat} and battery current I_{ba}, when the DC load changes. U_{bat} changes little because the battery voltage is mainly determined by the ideal voltage source inside. Figure 20c shows the waveforms, and when the illumination intensity decreases, the PV current I_{pv} decreases as a result. Then, the MPPT arithmetic works, I_{pv} increases and PV voltage U_{pv} decreases to reach the new maximum power point.

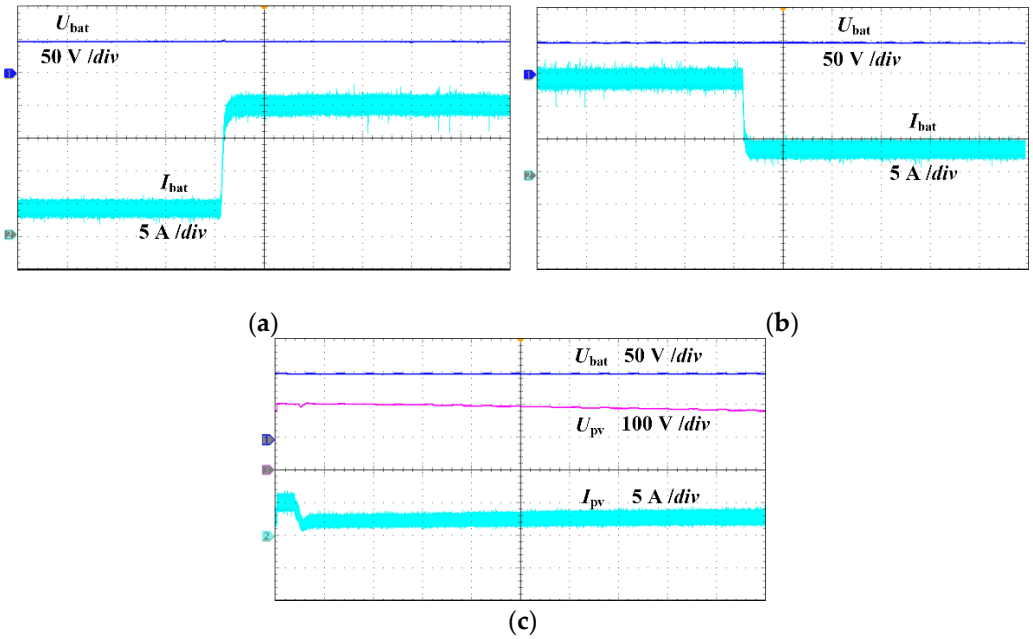


Figure 20. Waveforms in Battery/PV test system: (**a**) battery output current increases with the increase of load; (**b**) battery output current declines with the decrease of load; (**c**) regulating process when illumination intensity decreases.

6. Conclusions

A novel 400 V–50 V bidirectional DHC-LT converter is proposed in this paper. The topology structure and operation principles are discussed in detail. By moving the resonant capacitor from the LVS to the HVS, the volume and the conduction loss of the DHC-LT converter are decreased, the ZVS + ZCS characteristics are reserved, and a wide voltage range is obtained as well, which is proved by simulation. The Bode plot of the DHC-LT converter shows the converter is robust and suitable for DC power use of buildings and microgrids. To increase the accuracy of the FHA in the DHC-LT converter, the error factor of the FHA in resonant converters is analyzed, which are the AC output resistance and the phase angle. Then, an equivalent AC impedance model of the rectifier valid for DCM is proposed. By exacting FHA components from the output voltage and rectifier current, the phase angle of the AC impedance is taken into consideration. Therefore, the behavior in the resonant tank is described more precisely; the biggest relative error of voltage gain in step-down mode is around 9%, and that in step-up mode is around 10%, which is clearly lower than that of traditional FHA. The improved FHA method is proved to be effective. Then, a 2.5 kW DHC-LT prototype is established in the lab. The waveforms in CCM and DCM are presented, and the operation principles are confirmed. The peak efficiency is 97.3% in step-down mode, while the peak efficiency is 97.4% in step-up mode. By moving the resonant capacitor, the efficiency increases compared to the CDT-LC. A fixed-frequency phase-shift strategy is adopted to reduce the voltage gain, while ZVS is reserved by setting the dead time and the phase-shift angle reasonably. Finally, a battery/PV test system is established to verify the effectiveness of the DHC-LT converter in DC buildings and community microgrids.

Author Contributions: Conceptualization, methodology, validation and writing—original draft preparation are done by S.Z. Writing—review and editing and supervision are done by X.W. Validation is done by Z.Z. Software is done by X.Z. All authors have read and agreed to the published version of the manuscript.

Funding: This research received no external funding.

Conflicts of Interest: The authors declare no conflict of interest.

Appendix A

1. Open-loop transfer function of the DHC-LT converter.

$$\frac{\hat{u}_{\mathrm{L}}}{\hat{\omega}_{\mathrm{s}}} = \frac{2.64\times10^{-12}s^{11}+0.032s^{10}+26488.05s^{9}+2.64\times10^{11}s^{8}+4.96\times10^{17}s^{7}+3.02\times10^{23}s^{6}+1.28\times10^{30}s^{5}+1.67\times10^{35}s^{4}+1.00\times10^{42}s^{3}+1.41\times10^{47}s^{2}+1.78\times10^{53}s+2.81\times10^{58}}{s^{11}+1.42\times10^{6}s^{10}+4.21\times10^{12}s^{9}+4.56\times10^{18}s^{8}+5.33\times10^{24}s^{7}+4.53\times10^{30}s^{6}+2.47\times10^{36}s^{5}+1.57\times10^{42}s^{4}+3.52\times10^{47}s^{3}+1.74\times10^{53}s^{2}+5.14\times10^{56}s+1.96\times10^{61}} \quad \text{(A1)}$$

2. Derivation of U_{CD} and I_{CD} in step-down mode.

In Interval C of step-down mode, i_{AB} is approximately constant. Its value remains near the value of i_{AB} in T_{main} and $i_{AB}(T_{main})$. Because the calculation of $i_{AB}(T_{main})$ is complicated, it is estimated by half of the peak input current in the HVS resonant tank.

To facilitate the calculation, M_{rSD} is defined as the voltage ratio at the main resonant frequency in step-down mode. The M_{rSD} is obtained by the traditional FHA method when the switching frequency is equal to the main resonant frequency.

$$M_{\mathrm{rSD}} = \frac{U_{\mathrm{L}}}{U_{\mathrm{H}}} \quad \text{(A2)}$$

In Interval C, u_{Cr2} remains almost unchanged.

$$u_{\mathrm{Cr2}}(T_{\mathrm{main}}) = u_{\mathrm{Cr2}}(T_{\mathrm{s}}/2) = -u_{\mathrm{Cr2}}(0) \quad \text{(A3)}$$

$$C_{\mathrm{r2}}\left[u_{\mathrm{Cr2}(}T_{\mathrm{main}})-u_{\mathrm{Cr2}}(0)\right] = \int_0^{T_{\mathrm{main}}} i_{\mathrm{Cr2}}\,dt = \frac{1}{n_1}\int_0^{T_{\mathrm{main}}} i_{\mathrm{CD}}\,dt = \frac{U_{\mathrm{L}}T_{\mathrm{s}}}{2n_1R_{\mathrm{oSD}}} \quad \text{(A4)}$$

Thus

$$u_{\mathrm{Cr2}}(T_{\mathrm{main}}) = u_{\mathrm{Cr2}}(T_{\mathrm{s}}/2) = \frac{U_{\mathrm{L}}T_{\mathrm{S}}}{4n_1C_{\mathrm{r2}}R_{\mathrm{oSD}}} \quad \text{(A5)}$$

$$\int_0^{T_{\mathrm{main}}} i_{\mathrm{CD}}\,dt = \frac{U_{\mathrm{L}}T_{\mathrm{s}}}{2R_{\mathrm{oSD}}} \quad \text{(A6)}$$

In Interval C, i_{Lm1} and i_{Lm2} change a little, and i_{Lr} is small, so the voltage of magnetizing inductance L_{m1} and L_{m2} in the HVS, $u_{Lm1}(T_{main})$ and $u_{Lm2}(T_{main})$, can form the following equations.

$$\begin{cases} u_{\mathrm{Lm2}}(T_{\mathrm{main}}) - u_{\mathrm{Lm1}}(T_{\mathrm{main}}) = u_{\mathrm{Cr2}}(T_{\mathrm{main}}) \\ \frac{u_{\mathrm{Lm1}}(T_{\mathrm{main}})}{L_{\mathrm{m1}}} = -\frac{u_{\mathrm{Lm2}}(T_{\mathrm{main}})}{L_{\mathrm{m2}}} \end{cases} \quad \text{(A7)}$$

$u_{Lm1}(T_{main})$ and $u_{Lm2}(T_{main})$ can be expressed by

$$\begin{cases} u_{\mathrm{Lm1}}(T_{\mathrm{main}}) = (-L_{\mathrm{m2}}/L_{\mathrm{m1}} - 1)u_{\mathrm{Cr2}}(T_{\mathrm{main}}) \\ u_{\mathrm{Lm2}}(T_{\mathrm{main}}) = L_{\mathrm{m2}}(L_{\mathrm{m2}}/L_{\mathrm{m1}} + 1)/L_{\mathrm{m1}}\cdot u_{\mathrm{Cr2}}(T_{\mathrm{main}}) \end{cases} \quad \text{(A8)}$$

The output voltage of the resonant tank in T_{main} is

$$U_{\mathrm{SD}} = \frac{1}{n_1}u_{\mathrm{Lm1}}(T_{\mathrm{main}}) + \frac{1}{n_2}u_{\mathrm{Lm2}}(T_{\mathrm{main}}) \quad \text{(A9)}$$

As a result, u_{CD} can be described as

$$u_{\mathrm{CD}}(t) = \begin{cases} U_{\mathrm{L}} & 0 \le t < T_{\mathrm{main}} \\ U_{\mathrm{SD}} & T_{\mathrm{main}} \le t \le 1/(2f_{\mathrm{s}}) \end{cases} \quad \text{(A10)}$$

i_{CD} can be described as

$$i_{\mathrm{CD}}(t) = \begin{cases} I_{\mathrm{CD}}\ \sin(2\pi f_{\mathrm{r}}t) & 0 \le t < T_{\mathrm{main}} \\ 0 & T_{\mathrm{main}} \le t \le 1/(2f_{\mathrm{s}}) \end{cases} \quad \text{(A11)}$$

3. Derivation of U_{AB} and I_{AB} in step-up mode.

Just like List 2 of the Appendix A, it can be obtained that

$$u_{Cr1}(T_{main}) = u_{Cr1}(T_s/2) = \frac{1}{2C_{r1}}\int_0^{Tmain} i_{AB}\,dt = \frac{U_H T_S}{4C_{r1}R_{oSU}} \tag{A12}$$

To facilitate the calculation, M_{rSU} is defined as the voltage ratio at the main resonant frequency in step-up mode. The M_{rSU} is obtained by the traditional FHA method when the switching frequency is equal to the main resonant frequency in step-up mode.

$$M_{rSU} = \frac{U_H}{U_L} \tag{A13}$$

The average value of the input current is estimated by

$$i_{CD_avg} = \frac{U_H M_{rSU}}{R_{oSU}} \tag{A14}$$

The peak value of the input current is

$$i_{CD_pk} = \frac{\sqrt{2}k_{R_a}U_H M_{rSU}}{R_{oSU}} \tag{A15}$$

K_{R_a} is 1.1, which transforms the average value into an RMS value.

$$k_{R_a} = 1.1 \tag{A16}$$

Thus, $i_{CD}(T_{main})$ is estimated by half of i_{CD_avg}

$$i_{CD}(T_{main}) = \frac{\sqrt{2}k_{R_a}U_H M_{rSU}}{2R_{oSU}} \tag{A17}$$

It can be obtained that

$$\int_{T_{main}}^{Ts/2} i_{CD}\,dt = \frac{\sqrt{2}k_{R_a}U_H n_1 M_{rSU}T_s(f_r - f_s)}{4R_{oSU}f_r} \tag{A18}$$

$$\int_0^{T_{main}} i_{CD}\,dt = \frac{M_{rSU}U_H T_S}{2R_{oSU}} \tag{A19}$$

Therefore

$$\int_0^{Ts/2} i_{CD}\,dt = \frac{M_{rSU}U_H T_S}{2R_{oSU}} + \frac{\sqrt{2}k_{R_a}U_H n_1 M_{rSU}T_s(f_r - f_s)}{4R_{oSU}f_r} \tag{A20}$$

Thus

$$u_{Cr2}(T_s/2) = \frac{1}{2n_1C_{r2}}\int_0^{Ts/2} i_{CD}\,dt = \frac{M_{rSU}U_H T_S}{4n_1C_{r2}R_{oSU}} + \frac{\sqrt{2}k_{R_a}U_H M_{rSU}T_s(f_r - f_s)}{8C_{r2}R_{oSU}f_r} \tag{A21}$$

$$u_{Cr2}(T_{main}) = \frac{1}{2n_1C_{r2}}\int_0^{Tmain} i_{CD}\,dt = \frac{M_{rSU}U_H T_S}{4n_1C_{r2}R_{oSU}} \tag{A22}$$

To simplify the calculation, the value of u_{Cr2} in Interval C is the average of $u_{Cr2}(T_{main})$ and $u_{Cr2}(T_s/2)$ in the following part.

$$U_{Cr2_SU} = [u_{Cr2}(T_{main}) + u_{Cr2}(T_s/2)]/2 \tag{A23}$$

Thus, the voltage of magnetizing inductance L_{m1} and L_{m2} in the LVS, u'_{Lm1} and u'_{Lm2}, can form the following equations

$$\begin{cases} u'_{Lm1}(T_{main}) + u'_{Lm2}(T_{main}) = U_H / M_{rSU} \\ n_1 u'_{Lm1}(T_{main}) - n_2 u'_{Lm2}(T_{main}) = U_{Cr2_SU} \end{cases} \tag{A24}$$

u'_{Lm1} and u'_{Lm2} can be expressed by

$$\begin{cases} u'_{Lm1}(T_{main}) = \dfrac{n_2 U_H / M_{rSU} + U_{Cr2_SU}}{n_1 + n_2} \\ u'_{Lm2}(T_{main}) = d\dfrac{n_1 U_H / M_{rSU} - U_{Cr2_SU}}{n_1 + n_2} \end{cases} \tag{A25}$$

The current flowing through C_{r1} and L_r is 0, and as a result

$$u_{Lr}(T_{main}) = 0 \tag{A26}$$

The output voltage of the resonant tank in T_{main}, U_{SU} is

$$U_{SU} = u'_{Lm2}(T_{main}) - u_{Cr1}(T_{main}) \tag{A27}$$

As a result, u_{AB} can be described as

$$u_{AB}(t) = \begin{cases} U_H & 0 \le t < T_{main} \\ U_{SU} & T_{main} \le t \le 1/(2f_s) \end{cases} \tag{A28}$$

i_{AB} can be described as

$$i_{AB}(t) = \begin{cases} I_{AB}\ \sin(2\pi f_r t) & 0 \le t < T_{main} \\ 0 & T_{main} \le t \le 1/(2f_s) \end{cases} \tag{A29}$$

References

1. Xu, W.; Chan, N.H.L.; Or, S.W.; Ho, S.L.; Chan, K.W. A New Control Method for a Bi-Directional Phase-Shift-Controlled DC-DC Converter with an Extended Load Range. *Energies* **2017**, *10*, 1532. [CrossRef]
2. Yong, H.; Li, X.; Wu, X.; Li, M.; Wang, Y. Stability Control Design for TAB-Based Three-Port Bidirectional DC/DC Converters in PV-Battery Grid-Connected Applications. In Proceedings of the 46th Annual Conference of the IEEE Industrial Electronics Society (IECON 2020), Singapore, 18–21 October 2020; pp. 3469–3474.
3. Sha'aban, Y.A.; Ikpehai, A.; Adebisi, B.; Rabie, K.M. Bi-Directional Coordination of Plug-In Electric Vehicles with Economic Model Predictive Control. *Energies* **2017**, *10*, 1507. [CrossRef]
4. Fiaz, M.F.; Calligaro, S.; Iurich, M.; Petrella, R. Analytical Modeling and Control of Dual Active Bridge Converter Considering All Phase-Shifts. *Energies* **2022**, *15*, 2720. [CrossRef]
5. Onar, O.C. A Bidirectional High-Power-Quality Grid Interface With a Novel Bidirectional Noninverted Buck–Boost Converter for PHEVs. *IEEE Trans. Veh. Technol.* **2012**, *61*, 2018–2032. [CrossRef]
6. Chen, B.-Z.; Liao, H.; Chen, L.; Chen, J.-F. Design and Implementation of the Bidirectional DC-DC Converter with Rapid Energy Conversion. *Energies* **2022**, *15*, 898. [CrossRef]
7. Gierczynski, M.; Grzesiak, L.M.; Kaszewski, A. Cascaded Voltage and Current Control for a Dual Active Bridge Converter with Current Filters. *Energies* **2021**, *14*, 6214. [CrossRef]
8. He, P.; Khaligh, A. Comprehensive Analyses and Comparison of 1 kW Isolated DC–DC Converters for Bidirectional EV Charging Systems. *IEEE Trans. Transp. Electrif.* **2017**, *3*, 147–156. [CrossRef]
9. Wang, C.S.; Zhang, S.H.; Wang, Y.F.; Chen, B.; Liu, J.H. A 5-kW Isolated High Voltage Conversion Ratio Bidirectional CLTC Resonant DC–DC Converter With Wide Gain Range and High Efficiency. *IEEE Trans. Power Electron.* **2019**, *34*, 340–355. [CrossRef]
10. Can, E.; Sayan, H.H. Development of fractional sinus pulse width modulation with β gap on three step signal processing. *Int. J. Electron.* **2022**, 1–20. [CrossRef]
11. Zhao, B.; Song, Q.; Liu, W.; Sun, Y. Overview of Dual-Active-Bridge Isolated Bidirectional DC–DC Converter for High-Frequency-Link Power-Conversion System. *IEEE Trans. Power Electron.* **2014**, *29*, 4091–4106. [CrossRef]
12. Chen, G.; Lee, Y.S.; Hui, S.Y.R.; Xu, D.; Wang, Y. Actively clamped bidirectional flyback converter. *IEEE Trans. Ind. Electron.* **2000**, *47*, 770–779. [CrossRef]
13. Li, H.; Peng, F.Z.; Lawler, J.S. A natural ZVS medium-power bidirectional DC-DC converter with minimum number of devices. *IEEE Trans. Ind. Appl.* **2015**, *39*, 525–535. [CrossRef]

14. Cui, S.; He, D.; Chen, Z.; Habetler, T.G. A Wide Input Voltage Range ZVS Isolated Bidirectional DC-DC Converter for Ultra-capacitor Application in Hybrid and Electric Vehicles. In Proceedings of the 2012 IEEE International Electric Vehicle Conference, Greenville, SC, USA, 4–8 March 2012; pp. 1–6.
15. Roggia, L.; Costa, P.F.S. Comparative analysis between integrated full-bridge-forward and dual active bridge DC–DC converters. *Electron. Lett.* **2018**, *54*, 231–233. [CrossRef]
16. Núñez, R.O.; Oggier, G.G.; Botterón, F.; Garcia, G.O. Analysis of the Transformer Influence on a Three-Phase Dual Active Bridge DC-DC Converter. *IEEE Lat. Am. Trans.* **2016**, *14*, 3048–3055. [CrossRef]
17. Jin, K.; Liu, C. A Novel PWM High Voltage Conversion Ratio Bidirectional Three-Phase DC/DC Converter With Y–Δ Connected Transformer. *IEEE Trans. Power Electron.* **2015**, *31*, 81–88. [CrossRef]
18. Lee, S.; Park, J.; Choi, S. A Three-Phase Current-Fed Push–Pull DC–DC Converter With Active Clamp for Fuel Cell Applications. *IEEE Trans. Power Electron.* **2011**, *26*, 2266–2277. [CrossRef]
19. Min, J.; Ordonez, M. Bidirectional Resonant CLLC Charger for Wide Battery Voltage Range: Asymmetric Parameters Methodology. *IEEE Trans. Power Electron.* **2021**, *36*, 6662–6673. [CrossRef]
20. Jung, J.H.; Kim, H.S.; Ryu, M.H.; Baek, J.W. Design Methodology of Bidirectional CLLC Resonant Converter for High-Frequency Isolation of DC Distribution Systems. *IEEE Trans. Power Electron.* **2012**, *28*, 1741–1755. [CrossRef]
21. Lin, F.; Zhang, X.; Li, X.; Chaohui, L.; Ma, H. Parameter Design for Symmetrical CLLC-Type DC Transformer Considering Cascaded System Stability and Power Efficiency. *IEEE J. Emerg. Sel. Top. Power Electron.* **2020**, *9*, 6219–6231. [CrossRef]
22. Li, X.; Huang, J.; Ma, Y.; Wang, X.; Yang, J.; Wu, X. Unified Modeling, Analysis, and Design of Isolated Bidirectional CLLC Resonant DC-DC Converters. *IEEE J. Emerg. Sel. Top. Power Electron.* **2022**, *10*, 213–223. [CrossRef]
23. Ibanez, F.; Echeverria, J.M.; Fontan, L. Novel technique for bidirectional series-resonant DC/DC converter in discontinuous mode. *IET Power Electron.* **2013**, *6*, 1019–1028. [CrossRef]
24. Jiang, T.; Zhang, J.; Wu, X.; Sheng, K.; Wang, Y. A Bidirectional LLC Resonant Converter with Automatic Forward and Backward Mode Transition. *IEEE Trans. Power Electron.* **2014**, *30*, 757–770. [CrossRef]
25. Musavi, F.; Craciun, M.; Gautam, D.S.; Eberle, W. Control Strategies for Wide Output Voltage Range LLC Resonant DC–DC Converters in Battery Chargers. *IEEE Trans. Veh. Technol.* **2014**, *63*, 1117–1125. [CrossRef]
26. Çalışkan, E.; Ustun, O. Smart Efficiency Tracking for Novel Switch—LLC Converter for Battery Charging Applications. *Energies* **2022**, *15*, 1861. [CrossRef]
27. Chang, C.; Cheng, C.; Cheng, H. Modeling and Design of the LLC Resonant Converter Used as a Solar-Array Simulator. *IEEE J. Emerg. Sel. Top. Power Electron.* **2014**, *2*, 833–841. [CrossRef]
28. Zhang, S.-H.; Wang, Y.-F.; Chen, B.; Han, F.-Q.; Wang, Q.-C. Studies on a Hybrid Full-Bridge/Half-Bridge Bidirectional CLTC Multi-Resonant DC-DC Converter with a Digital Synchronous Rectification Strategy. *Energies* **2018**, *11*, 227. [CrossRef]
29. Chen, B.; Wang, P.; Wang, Y.F.; Zhang, S.H.; Yang, L.; Ji, R.L. A Bidirectional CDT-LC Resonant DC-DC Converter with a Wide Voltage Range. *IEEE Trans. Ind. Electron.* **2020**, *67*, 2009–2020. [CrossRef]
30. Ma, X.; Wang, P.; Bi, H.; Wang, Z. A Bidirectional LLCL Resonant DC-DC Converter With Reduced Resonant Tank Currents and Reduced Voltage Stress of the Resonant Capacitor. *IEEE Access* **2020**, *8*, 125549–125564. [CrossRef]
31. Liu, T.; Zhou, Z.; Xiong, A.; Zeng, J.; Ying, J. A Novel Precise Design Method for LLC Series Resonant Converter. In Proceedings of the INTELEC 06—Twenty-Eighth International Telecommunications Energy Conference, Providence, RI, USA, 10–14 September 2006; pp. 1–6.
32. Can, E. The design and experimentation of the new cascaded DC-DC boost converter for renewable energy. *Int. J. Electron.* **2019**, *106*, 1374–1393. [CrossRef]
33. Hu, Z.; Wang, L.; Wang, H.; Liu, Y.F.; Sen, P.C. An Accurate Design Algorithm for LLC Resonant Converters—Part I. *IEEE Trans. Power Electron.* **2016**, *31*, 5435–5447. [CrossRef]
34. Hu, Z.; Wang, L.; Qiu, Y.; Liu, Y.F.; Sen, P.C. An Accurate Design Algorithm for LLC Resonant Converters—Part II. *IEEE Trans. Power Electron.* **2016**, *31*, 5448–5460. [CrossRef]
35. Steigerwald, R.L. A Comparison of Half-bridge Resonant Converter Topologies. *IEEE Trans. Power Electron.* **2002**, *3*, 174–182. [CrossRef]
36. Ivensky, G.; Bronshtein, S.; Abramovitz, A. Approximate Analysis of Resonant LLC DC-DC Converter. *IEEE Trans. Power Electron.* **2011**, *26*, 3274–3284. [CrossRef]
37. Liu, J.; Zhang, J.; Zheng, T.Q.; Yang, J. A Modified Gain Model and the Corresponding Design Method for an LLC Resonant Converter. *IEEE Trans. Power Electron.* **2017**, *32*, 6716–6727. [CrossRef]
38. Abdel-Rahim, O.; Alamir, N.; Abdelrahem, M.; Orabi, M.; Kennel, R.; Ismeil, M.A. A Phase-Shift-Modulated LLC-Resonant Micro-Inverter Based on Fixed Frequency Predictive-MPPT. *Energies* **2020**, *13*, 1460. [CrossRef]